

Load Evaluation of Debris Flow Against Steel Open Sabo Dam Using DEM

Toshiyuki Horiguchi^{1*}, Yoshiharu Komatsu¹, Satoshi Katsuki¹
and Nobutaka Ishikawa²

¹ Dept. of Civil Eng., National Defense Academy, (1-10-20 Hashirimizu, Yokosuka, Kanagawa, 239-0811, Japan)

² Professor Emeritus of National Defense Academy, (1-10-20 Hashirimizu, Yokosuka, Kanagawa, 239-0811, Japan)

*Corresponding author. E-mail: htoshi@nda.ac.jp

Although latest statistics indicate a decrease in the number of victims of natural disasters in Japan, numbers of sediment disasters have actually increased. For instance, a torrential downpour hit the mountain areas of northern Kyusyu in July 2017, and this caused loss of life and damage to property. Development of sediment control structures is necessary for countering sediment and debris flow disasters. One of such counter measures is steel open type check dam (hereafter, steel open Sabo dam). By utilizing segregation mechanism of boulders in a debris flow, the steel open dam is expected to capture them. When the debris flow attacks the steel open Sabo dam, huge impact load occurs between boulders and steel pipes. Therefore, it is very significant to evaluate the debris flow load of steel open Sabo dam from the design point of view. This paper presents experimental and computational approaches to impact load of debris flow including boulders hitting the steel open Sabo dam. First, debris flow experiments are carried out by using 1/40 scale channel slope, and the impact load is measured by using a load cell. Second, the distinct element method is used for a simulation analysis of the model test. Herein, the computational results show good reproducibility of experiments. This debris flow load analysis will be very useful for the safety assessment of steel open dam against rock impact in the debris flow.

Key words: Steel open Sabo dam, impact load, DEM, simulation, debris flow

1. INTRODUCTION

Although latest statistics indicate a decrease in the number of victims by natural disasters in Japan, there has been an increase in the number of sediment disasters. In addition, the latest worldwide statistics of a natural disaster such as typhoons, tsunamis, floods, avalanches, landslides, debris flows and earthquakes indicate that the number of victims is increasing. Among those problems, debris flow hazards have increased removal costs of debris flows from dam reservoir or general damage to dam sites. One of such countermeasures is the steel open type check dam (hereafter, steel open Sabo dam) as shown in **Photo 1**, which is composed of steel pipes. They are designed to allow sand and gravels to pass downstream through open spaces. But, when the debris flow occurs, the steel open Sabo dams are expected to capture huge rocks and/or boulders which are concentrated in a front part of debris flow, and the following gravels and sand [Sabo & Landslide Technical Center, 2016]. During the process to capture the boulders, the steel pipes are directly hit by huge boulders, then large impact loads



Photo 1 Steel open Sabo dam

occur between boulders and steel pipes. Then the impact load sometimes breaks the pipes. Therefore, the impact load evaluation of steel open Sabo dam is very significant from the design point of view.

There are research works discussing debris flow load evaluation including boulder impact. Ikeya³ et. al., classified the type of debris flow model by means of fluid theory and also solid state theory, which disposes of the system of the impact load [Ikeya;1987]. Mizuyama investigated the method of impact load estimation on concrete dam using two

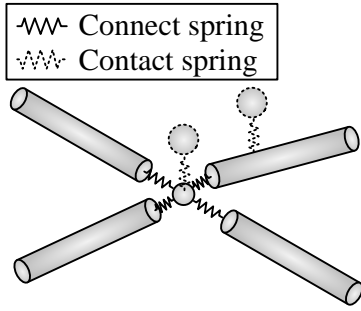


Fig. 1 Structural model

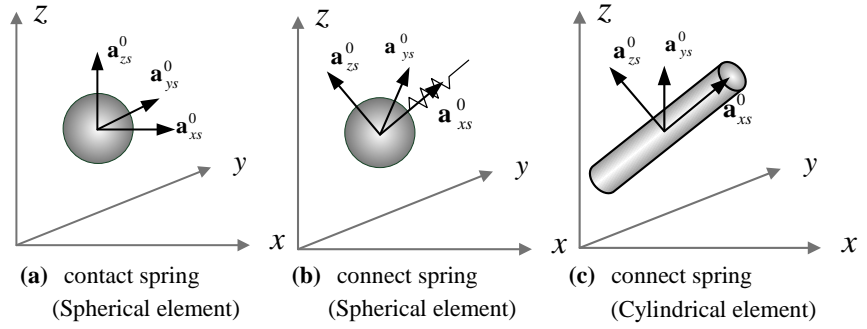


Fig. 2 Initial posture of element and spring

characteristic debris flow, which utilizes fluid theory [Mizuyama; 1987]. Among them, focusing on the load due to the collision of the boulder, local failure energy in a collision is estimated. This technique is adopted in the design manual [Sabo & Landslide Technical Center, 2016].

Miyoshi et al., carried out the Sabo dam experiment on impact load evaluation in the unsteady jet [Miyoshi; 1990]. Consequently, the mechanism of impact which occurs debris flow against Sabo dam was clarified. Daido et al., evaluated the pressure of mud-debris flow acting on a flat face of the dam [Daido; 1994]. The debris flow was regarded as a non-compressible fluid or as a tiny-compressible fluid. Yamamoto et al., discussed impact load caused by debris flow on a Sabo dam by DEM analysis [Yamamoto; 1998]. The impact load experiment was performed for the wall type dam. And those are analysed by the modified DEM analysis which takes into account the rolling resistant moment buoyancy and drag force of water. Ishikawa et al., investigated the impulsive load of debris flow by using pumice stones in the channel flume and simulated it by using smoothed particle hydrodynamics [Ishikawa; 2009]. However, the study on the debris flow load acting on a steel open dam has not been carried out sufficiently.

This paper presents experimental and computational approaches to impact load of debris flow including boulders against the open type check dam. First, the debris flow experiments are carried out by using 1/40 scale channel, and the impact loads are measured by using a load cell. Second, DEM is used for a simulation analysis of the model test.

2. DEM SIMULATION AND LOAD EVALUATION

2.1 Outline of distinct element method

The DEM normally uses spherical model. Contact judgement between the elements are done each time. If one element contacts with another element, a spring action is generated between the elements and that equation of motion is solved based

on the contact force.

2.2 Contact spring and connect spring

Fig. 1 shows an image of the contact spring and the connect spring. The functions of the connect spring and the contact spring have a little difference. If a spherical element touches the cylindrical element, then the contact spring between two elements is set. On the other hand, the connect spring is set between two cylindrical elements at the beginning. In addition, the spring is always kept between those elements. Moreover, the position and direction of the contact spring at the action point was updated based on the combination and position of those elements, and removed by contact judgement. On the other hand, the connect spring is fixed at the connected elements. Updating manner of those spring deformation and force is described later.

2.3 Displacement and posture matrix of element

A spherical element with contact spring function in the global coordinate system and the local coordinate system is shown in Fig. 2 (a). The direction of the connected spring is assumed to be the local x -coordinate of the local coordinate system, and the posture matrix that has y direction vector of the xy plane of the global coordinate system is used as shown in Fig. 2 (b). In this study, the following relation has been applied to denote the posture matrix at each point in time:

$$\mathbf{A}_s = \begin{bmatrix} \mathbf{a}_{xs}^T \\ \mathbf{a}_{ys}^T \\ \mathbf{a}_{zs}^T \end{bmatrix} = \mathbf{T}_s \mathbf{A} \quad (1)$$

where \mathbf{A}_s : posture matrix corresponding to connect spring of spherical element, \mathbf{T}_s : coordinate conversion matrix for converting posture matrix \mathbf{A} to \mathbf{A}_s , that denotes the spherical element, and \mathbf{a}_{xs} , \mathbf{a}_{ys} , \mathbf{a}_{zs} : x , y , z of posture matrix corresponding to connect spring of spherical element \mathbf{A}_s .

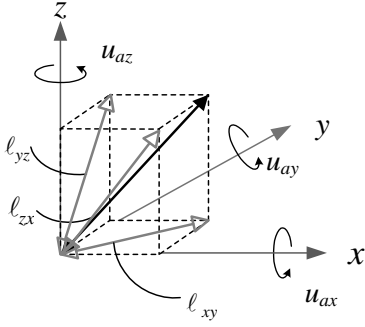


Fig. 3 Renewal of posture matrix

In addition, the x coordinate in the local coordinate system is specified as the central axis of the cylindrical element as shown in Fig. 2 (c). Initial posture matrix coordinates are parallel to the specified global coordinate system. The following procedure is conducted for updating the posture matrix. The posture matrix is a matrix composed of the direction cosine vector and with unit vector length.

Here, the posture matrix of connect spring is assumed to be updated by the following approximate solutions with reference to Fig. 3:

$$x_{ax}(t + \Delta t) = l_{xy} \cdot \cos\left\{\tan^{-1}\left(\frac{y_{ax}}{x_{ax}}\right) + \Delta u_{ax}\right\} + l_{zx} \cdot \sin\left\{\tan^{-1}\left(\frac{x_{ax}}{z_{ax}}\right) + \Delta u_{ay}\right\} + x_{ax}(t) \quad (2a)$$

$$y_{ax}(t + \Delta t) = l_{yz} \cdot \cos\left\{\tan^{-1}\left(\frac{z_{ax}}{y_{ax}}\right) + \Delta u_{ax}\right\} + l_{xy} \cdot \sin\left\{\tan^{-1}\left(\frac{y_{ax}}{x_{ax}}\right) + \Delta u_{az}\right\} + y_{ax}(t) \quad (2b)$$

$$z_{ax}(t + \Delta t) = l_{zx} \cdot \cos\left\{\tan^{-1}\left(\frac{x_{ax}}{z_{ax}}\right) + \Delta u_{ay}\right\} + l_{yz} \cdot \sin\left\{\tan^{-1}\left(\frac{z_{ax}}{y_{ax}}\right) + \Delta u_{ax}\right\} + z_{ax}(t) \quad (2c)$$

where l_{xy} , l_{yz} and l_{zx} : length of the vector \mathbf{a}_x at time t projected to xy , yz , zx plane as indicated in Fig. 3: x_{ax} , y_{ax} , z_{ax} : x , y , z direction elements of \mathbf{a}_x at time t ; Δu_{ax} , Δu_{ay} , Δu_{az} : incremental quantity of rotation angle vector \mathbf{u}_a along x , y , z directions in the incremental time Δt , respectively.

Therefore, \mathbf{a}_x , \mathbf{a}_y , \mathbf{a}_z are obtained as follows.

$$\mathbf{a}_x(t + \Delta t) = \frac{1}{\sqrt{(x_{ax}(t + \Delta t))^2 + (y_{ax}(t + \Delta t))^2 + (z_{ax}(t + \Delta t))^2}} \begin{bmatrix} x_{ax}(t + \Delta t) \\ y_{ax}(t + \Delta t) \\ z_{ax}(t + \Delta t) \end{bmatrix} \quad (3a)$$

$$\mathbf{a}_y(t + \Delta t) = \frac{1}{\sqrt{(x_{ay}(t + \Delta t))^2 + (y_{ay}(t + \Delta t))^2 + (z_{ay}(t + \Delta t))^2}} \begin{bmatrix} x_{ay}(t + \Delta t) \\ y_{ay}(t + \Delta t) \\ z_{ay}(t + \Delta t) \end{bmatrix} \quad (3b)$$

$$\mathbf{a}_z(t + \Delta t) = \mathbf{a}_x(t + \Delta t) \times \mathbf{a}_y(t + \Delta t) \quad (3c)$$

2.4 Equation of motion

The equation of motion considering the damping effect in the DEM is usually expressed as follows.

$$\mathbf{M}\ddot{\mathbf{u}}_t + \mathbf{D}\dot{\mathbf{u}}_t + \mathbf{f}_K\mathbf{u}_t = \mathbf{f}_t \quad (4)$$

where \mathbf{M} : mass matrix, \mathbf{D} : damping matrix, \mathbf{f}_K : internal force vector caused by contact spring force or connect spring force, \mathbf{f} : external force vector, \mathbf{u} :

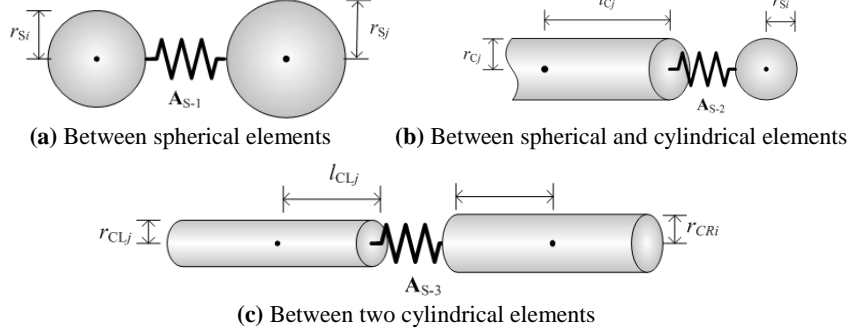


Fig. 4 Each of connect spring

displacement vector, and (\cdot) , $(\ddot{\cdot})$: each of the first or second derivatives of time, respectively.

2.5 Equilibrium condition

Equilibrium in the connect spring between the spherical and cylindrical elements is illustrated by the structural model in Fig.1. Herein, the direction of the compression force is considered as the x -axis. The connect spring between two spherical elements is illustrated in Fig. 4 (a). The connect spring between the spherical and cylindrical elements is illustrated in Fig. 4 (b). The connect spring between two cylindrical elements is illustrated in Fig. 4 (c).

Then, the equilibrium of forces is converted into the spring force in the global coordinate by considering connect spring of element in local coordinate as follows:

$$\tilde{\mathbf{S}}_n = \mathbf{T}_{ns}\mathbf{S}_c \quad (5)$$

where $\tilde{\mathbf{S}}_n$: force vector in the spring local coordinate, \mathbf{S}_c : force vector in connected spring, \mathbf{T}_{ns} : a geometric transformation matrix.

By using posture matrix \mathbf{A}_n of the element and posture matrix \mathbf{A}_s of connected spring, \mathbf{T}_{ns} is given by the following equation:

$$\mathbf{T}_{ns} = \mathbf{A}_n\mathbf{A}_s^T = \begin{bmatrix} \mathbf{a}_{xn}^T \\ \mathbf{a}_{yn}^T \\ \mathbf{a}_{zn}^T \end{bmatrix} \begin{bmatrix} \mathbf{a}_{xs}^T \\ \mathbf{a}_{ys}^T \\ \mathbf{a}_{zs}^T \end{bmatrix}^T = \begin{bmatrix} \mathbf{a}_{xn}^T\mathbf{a}_{xs} & \mathbf{a}_{xn}^T\mathbf{a}_{ys} & \mathbf{a}_{xn}^T\mathbf{a}_{zs} \\ \mathbf{a}_{yn}^T\mathbf{a}_{xs} & \mathbf{a}_{yn}^T\mathbf{a}_{ys} & \mathbf{a}_{yn}^T\mathbf{a}_{zs} \\ \mathbf{a}_{zn}^T\mathbf{a}_{xs} & \mathbf{a}_{zn}^T\mathbf{a}_{ys} & \mathbf{a}_{zn}^T\mathbf{a}_{zs} \end{bmatrix} \quad (6)$$

where \mathbf{a}_{xn} , \mathbf{a}_{yn} , \mathbf{a}_{zn} : vector of each unit coordinate axis that comprises posture matrix of element assuming $n = L$ (Left side) or $n = R$ (Right side).

The equilibrium condition is expressed as follows:

$$\tilde{\mathbf{f}}_L = \tilde{\mathbf{C}}_L^T\tilde{\mathbf{S}}_L \quad (7a)$$

$$\tilde{\mathbf{f}}_R = \tilde{\mathbf{C}}_R^T\tilde{\mathbf{S}}_R \quad (7b)$$

where $\tilde{\mathbf{f}}_L$, $\tilde{\mathbf{f}}_R$: each external force vector of the element of posture matrix in the coordinate system, $\tilde{\mathbf{S}}_L$, $\tilde{\mathbf{S}}_R$: spring force vector at the point of action according to the posture matrix \mathbf{A}_n , $\tilde{\mathbf{C}}_L^T$, $\tilde{\mathbf{C}}_R^T$:

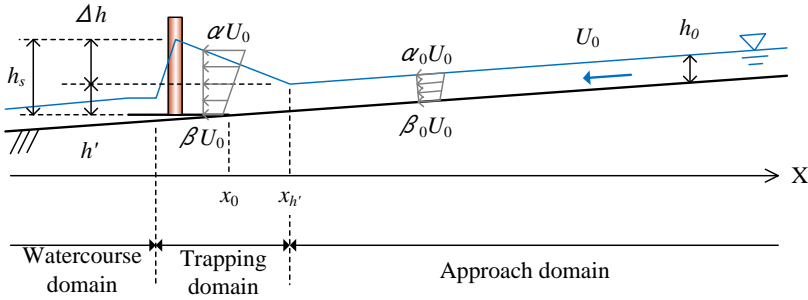


Fig. 5 Water flow domain model

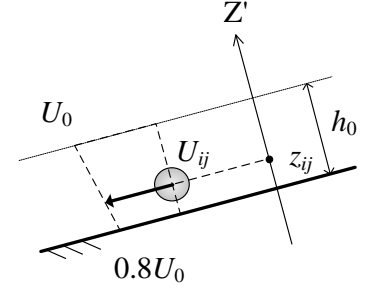


Fig. 6 Velocity distribution in approach domain

equilibrium matrix of the local coordinate system.

In addition, the local coordinate force is converted into the global coordinate system by the following equation:

$$\mathbf{f}_{Kn} = \mathbf{T}_{Gn} \tilde{\mathbf{f}}_n \quad (8)$$

where \mathbf{f}_{Kn} : force vector of gravity of the element n in the global coordinate system, $\tilde{\mathbf{f}}_n$: point gravity force vector according to posture matrix \mathbf{A}_n , \mathbf{T}_{Gn} : $n = L$ or $n = R$ is a coordinate transformation matrix converted from local coordinate system to global coordinate system. The transformation matrix is expressed as follows:

$$\mathbf{T}_{Gn} = \begin{bmatrix} \mathbf{x}_G^T \mathbf{a}_{xn} & \mathbf{x}_G^T \mathbf{a}_{yn} & \mathbf{x}_G^T \mathbf{a}_{zn} \\ \mathbf{y}_G^T \mathbf{a}_{xn} & \mathbf{y}_G^T \mathbf{a}_{yn} & \mathbf{y}_G^T \mathbf{a}_{zn} \\ \mathbf{z}_G^T \mathbf{a}_{xn} & \mathbf{z}_G^T \mathbf{a}_{yn} & \mathbf{z}_G^T \mathbf{a}_{zn} \end{bmatrix} \quad (9)$$

where $\mathbf{x}_G, \mathbf{y}_G, \mathbf{z}_G$: Vector of the whole coordinate system of unit coordinate axes.

Derived from eq. (5) to eq. (9), the following formula is obtained:

$$\mathbf{f}_{Kn} = \mathbf{T}_{Gn} \tilde{\mathbf{C}}_n^T \mathbf{T}_{ns} \mathbf{S}_c \quad (10)$$

2.6 Water flow model

The debris flow is composed of boulders, cobbles, and water flow. Therefore, it is necessary to assume the water flow model which affects as driving force of the debris. The water flow velocity around debris flow changes owing to the interactive action of debris motion. However, this interaction is ignored in this study to reduce the computational load. Accordingly, the water flow model is adapted to two different domains in this study, as shown in Fig. 5.

2.6.1 Approach domain

In the approach domain, as shown in Fig.6, water flows parallel to the bottom surface of the channel. And the velocity changes proportionally in depth as follows:

$$\mathbf{U}_d = U \left(1 - 0.2 \frac{d}{h_0} \right) \quad (0 \leq d \leq h_0) \quad (11)$$

where U : water velocity at the surface, \mathbf{U}_d : water velocity vector at depth d , d : depth of related drift wood element, and h_0 : depth of water in approach domain.

The water depth is obtained from experimental observations. The surface velocity is determined such that the integration of these velocities for a section area of the water flow should be equivalent to the experimental discharge.

2.6.2 Trapping domain

The water depth in the trapping domain increase proportionally closing to the steel open dam as shown in Fig. 6. The depth of debris flow at the steel open dam is given by the ratio of the projection area of the captured drift woods and the cross-sectional area of the water flow, as shown in Fig. 7 as follows:

$$\begin{cases} h' = h_0 & (\sum A_{di}/A_0 \leq 0.2) \\ h' = \frac{H-h_0}{1.3} \left(\frac{\sum A_{di}}{A_0} - 0.2 \right) + h_0 & (0.2 \leq \sum A_{di}/A_0 \leq 1.5) \\ h' = H & (1.5 \leq \sum A_{di}/A_0) \end{cases} \quad (12)$$

where H : height of the anti-drift-wood structure, \mathbf{A}_{di} : the sum of the captured drift woods projection area, and A_0 : cross-sectional area of the water flow.

The cross-sectional average velocity \bar{U} is given by the depth h' based on the law of conservation of discharge as follows.

$$\bar{U} = \frac{h_0}{h'} U \quad (13)$$

The increment of the damping-up depth Δh is given as follows:

$$\Delta h = k_m \sin \theta_m \left(\frac{D}{W} \right) \frac{U_h}{2g} \quad (14)$$

where k_m : section modules, θ_m : angle of capturing columns to bottom, D : diameter capturing columns, W : a gap of capturing columns, and U_h : upstream water velocity.

Furthermore, considering the turbulence and waves of the water surface, the damping-up depth h_s is given by a random number according to the normal distribution, as shown in Fig. 8. Then, the maximum h_s is $h'+\Delta h$, the average of h_s is $h'+\Delta h/2$, and the

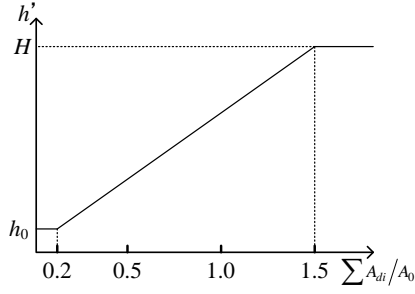


Fig. 7 Depth and relative area

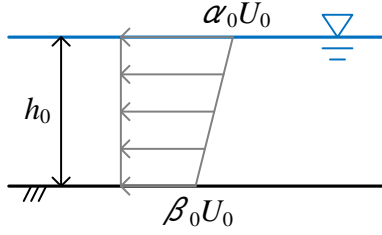


Fig. 9 Velocity distribution in trapping domain

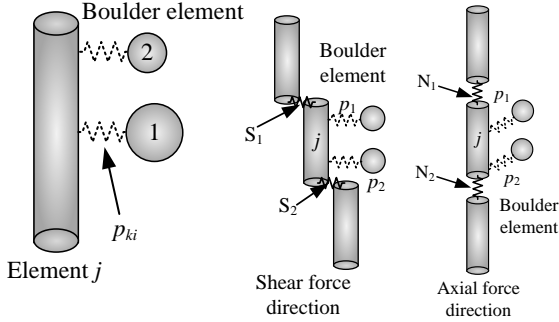


Fig. 11 Load evaluation (member)

standard deviation of h_s is defined as $\Delta h/4$.

The velocity distribution in the trapping domain changes as shown in **Fig. 9**. To keep a constant discharge, the decrement coefficients α and β are given by coefficient γ based on the law of conservation of flow, respectively, as follows.

$$\alpha = \alpha_0 + \gamma \quad (15)$$

$$\beta = \beta_0 - 2\gamma \quad (16)$$

$$\gamma = \frac{1}{3} \left(1 - \frac{h_0}{h'} \right) (\alpha_0 + \beta) \quad (17)$$

Therefore, the velocity in the trapping domain is given as follows.

$$U_d = \frac{d}{h'} (\alpha - \beta) \bar{U} + \beta \bar{U} \quad (18)$$

Finally, by considering the turbulence of water flow, the tangential direction velocity turbulent component U_z can be given by a random number according to the normal distribution as shown in **Fig. 10**. Then, the maximum of U_z is defined as $0.3U_d$, the minimum of U_z is $-0.3U_d$, the average of U_z is $-0.15U_d$, and the standard deviation of U_z is $0.3U_d/4$.

This velocity U_z is considered only in a

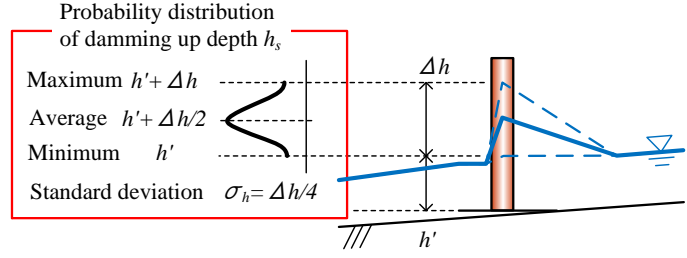


Fig. 8 Probability distribution of damming up depth h_s

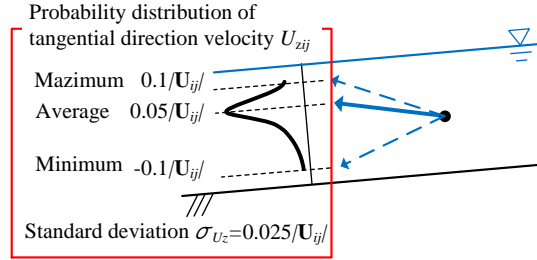


Fig. 10 Probability distribution of tangential direction velocity

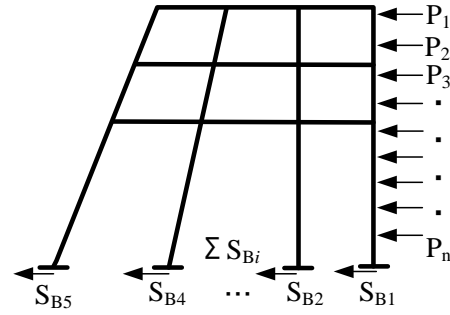


Fig. 12 Load evaluation (structure)

supercritical flow, and it is defined as follows:

$$\Delta h \leq h_c = 3 \sqrt{\frac{(h_0 U)^2}{g}} \quad (19)$$

where h_c : critical depth.

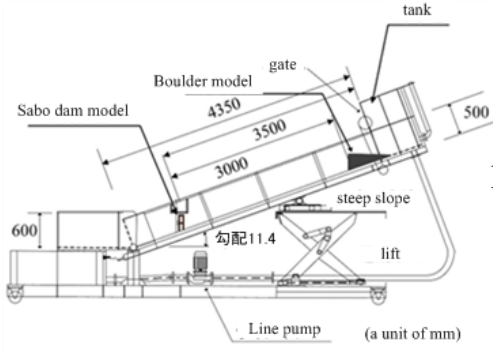
2.7 Evaluation of debris flow load on a steel open dam

DEM with proposed flow model can calculate the debris flow load by assembling contact forces between boulder elements and cylindrical elements as shown in **Fig. 11 (a)**. In case of contact with a number of boulder elements, as shown in **Fig. 11 (b)**, the debris flow load acting on j cylindrical element is calculated as follows:

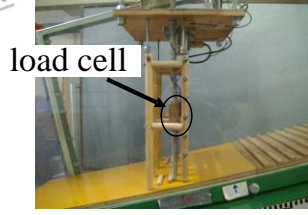
$$P_j = \sum_{i=1}^n p_{ki} \quad (20)$$

where P_j : the debris flows load acting on cylindrical element j , p_{ki} : the spring force between boulder element k and cylindrical element j .

The force of tangential direction is generated in the cylindrical elements. Then, the shear spring force



(a) Experimental flume



(b) Dam model

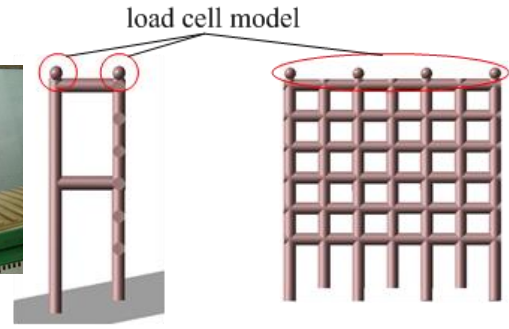


Fig. 14 Analytical dam model

Fig. 13 Outline of experimental setup

Table 1 Parameters of analysis

	item	value
Flux	Initial velocity U_0 (m/s)	2.0
	Initial depth h_0 (cm)	10
	Drag force C_D	0.49
Dam model	Cylindrical element	119
	Spherical element	8
Channel	Plane element	3
	Cylindrical element	26
	Slope θ	11.4°
Boulder model	Spherical element	1000
Interparticle	Normal spring constant K_n (N/m)	1.0×10^6
	Tangential spring constant K_s (N/m)	3.5×10^5
	Damping constant h	0.8
	Viscosity C	0
	Friction coefficient $\tan\phi$	0.466
Time increment Δt		1.0×10^{-6}

of the tip of cylindrical element j can be obtained as shown in Fig. 11 (b) as follows:

$$P_{Sj} = S_{1j} - S_{2j} \quad (21)$$

where P_{Sj} : the shearing force acting on the orthogonal directions of cylindrical element j , the S_{1j} , S_{2j} : shearing force acting on the tip of j cylindrical element.

The difference between axial forces acting on j cylindrical element is found as follows.

$$P_{Nj} = N_{1j} - N_{2j} \quad (22)$$

where P_{Nj} : the difference between two axial forces acting on both of tips of j cylindrical element in axial force direction, N_{1j} : the axial force of tip of j cylindrical element.

Finally, the whole debris flow load P_T is obtained by integrating the front contact force i and the shearing force of base element i as shown in Fig.12:

$$P_T = \sum_{i=1}^n P_i = \sum_{i=1}^n S_{Bi} \quad (23)$$

where P_T : the horizontal load acting overall structure, P_i : the contact force of boulder element i acting on each point to structure, S_{Bi} : the shearing force acting on the base element i of the dam, which

corresponds to the value of load cell as shown in Fig. 13, because the load was measured by load cell upside-down against the dam.

In order to examine the validity of this analytical approach, the model experiment is carried out to measure the impact load which is compared with computational results.

3. EXPERIMENTS OF OPEN DAM MODEL

Fig. 13 (a) shows the experimental set-up using channel flume, length of 4.35 m, width of 0.3 m and height of 0.5 m. Water flow is made by using a line pump and a cistern. The inclination of experimental flume was fixed at $\theta = 11.4^\circ$. The initial position of water is 3.5 m far from the dam model. The potentiometer is set at the top of open Sabo dam model to measure the impact load of debris flow.

The diameters of grains are from 30 to 40 mm (2.6 in the specific gravity) and the debris flow model is made by rushing water and gravels.

The dam model with height of 260 mm, width of 270 mm and depth of 90 mm is made as shown in Fig. 13 (b). This is 1/40 scale of a real steel open dam in which is made by a wooden column with a diameter

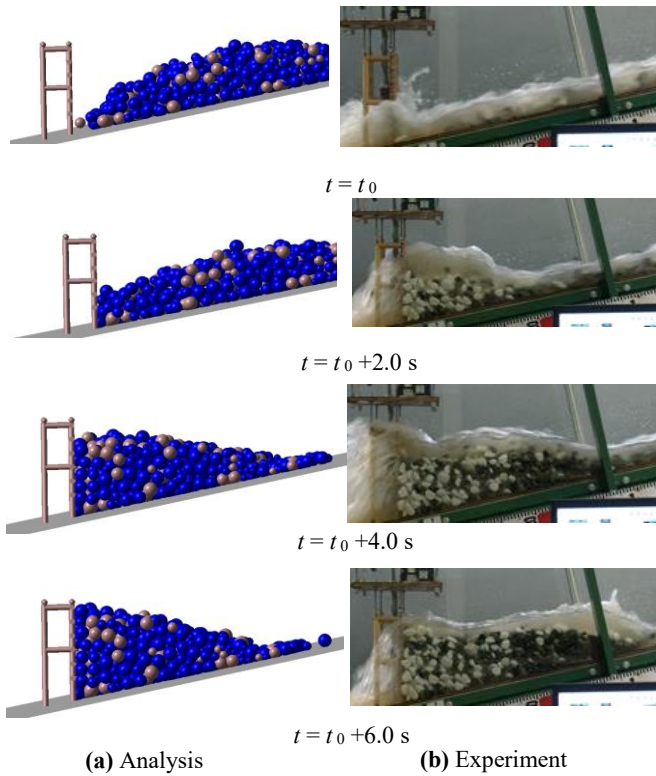


Fig. 15 Comparison of debris flow behavior

of 15 mm. Moreover, the steel open dam model is hung from the measurement trestle to measure the debris flow load by using the load cell.

4. ANALYSIS OF OPEN DAM MODEL

4.1 Analytical dam model

The analytical dam model is composed of cylindrical elements which are connected with springs between those elements as shown in Fig. 14. The load cell model is also connected with springs between spherical and cylindrical model at top of the structure, and the spring force is evaluated as impact load acting on the whole structure [Katsuki, 2012; Shibuya, 2012].

4.2 DEM parameter

The parameters used in the analysis are shown in Table 1. First, the depth and the flow velocity were identical to the experimental ones. The channel model is formed by using plane elements. The drag force $C_d = 0.49$ is adjusted to spherical and cylindrical shape. A spring constant ($K_n = 1.0 \times 10^6 \text{ N/m}$) is determined from boulder rigidity. The damping constant ($h = 0.8$), and the friction coefficient ($\phi = 25^\circ$) are also fit to experiment [Katsuki, 2012; Shibuya, 2012].

4.3 Computational and experimental results

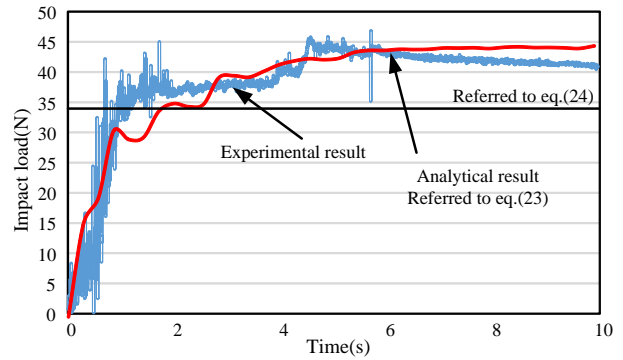


Fig. 16 Time history of debris flow load

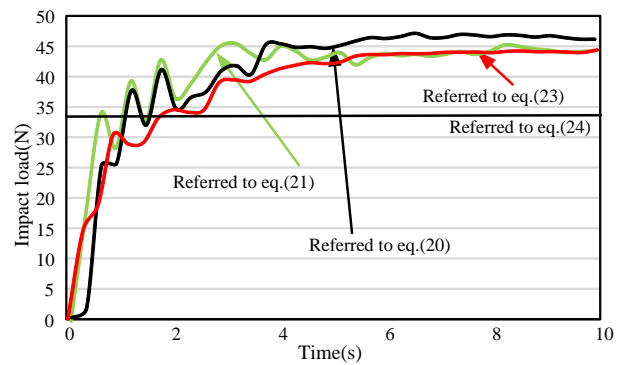


Fig. 17 Comparison of debris flow load

Fig. 15 (a) shows the computational results of debris flow behavior, in which the gravels are hitting to the dam model from the start time ($t = t_0$) to fill up the front space of the dam ($t = t_0 + 6.0$ s). In comparison, Fig. 15 (b) shows the experimental results of debris flow behavior at each time. Those behaviors show good agreement with each other at the same time.

Fig. 16 illustrates the time history of the debris flow load which is measured at back face of the dam in the experiment, and computational result by Eq. (24) in the analysis. The debris flow loads through the test and the analysis quickly increase more than 20 N at the time of 1.0 s, at which the front of debris flow hit the dam. Then, the loads gradually increase to 45 N until the time of 4.0 s, at which the front height of debris flow almost reaches the height of the dam, at the time ($t = t_0 + 6.0$ s) as shown in Fig. 15. After the time of 4.0 s, the loads keep the value of about 45 N.

Fig. 17 shows a comparison of loads obtained by Eqs. (20), (21), (23). Debris flow loads evaluated by using Eqs. (20), (21) are larger than one of Eq.(23). It is also found that the local forces integrated by Eqs. (20), (21) are much similar to the experimental one as shown in Fig. 16.

4.4 Comparison with design guideline

The design debris flow load is shown in Fig. 18. This formula is specified by the design guideline of Japan as follows [Sabo & Landslide Technical

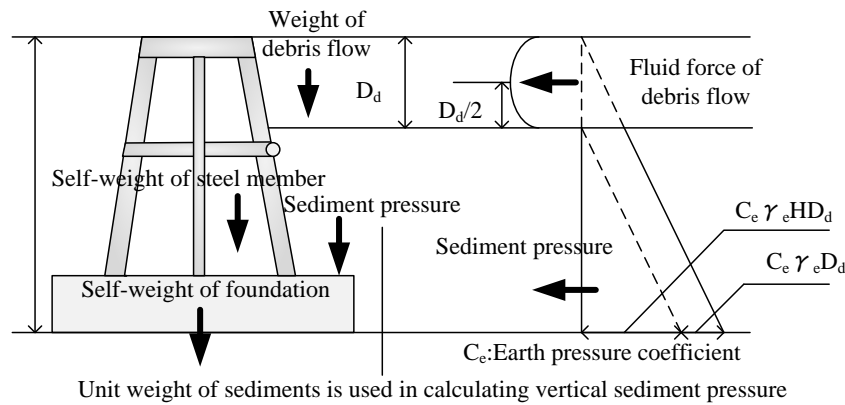


Fig. 18 design debris flow load [Osanai; 2010].

Center, 2016; Kiyomiya, 2003]. The design load is static sediment pressure and fluid force of debris flow. Here, the fluid force of debris flow is shown only below:

$$P_g = \frac{1}{2} C_e \gamma_e h^2 B \quad (24)$$

where, P_g : sediment sand pressure, C_e : coefficient of earth pressure ($\phi_e = 35^\circ$), γ_e : unit weight of debris flow (15.9 kN/m^3), h : height from sediment sand, B : channel width.

The load P_g is obtained as 34 N by using experimental parameters and this value is indicated as shown in **Fig. 15** by a brown line. Therefore, it was recognized that loads of experiment and simulation are 1.3 times as large as one of Eq. (24).

5. CONCLUSION

This paper presents experimental and computational approaches to impact load of debris flow including boulders against the steel open dam. After the front part of debris flow hit the structure, the load quickly increases to the maximum value, and keeps this value over the whole experiment time. DEM can simulate gravels' behaviors around the structure and time history of the impact load very well.

Therefore, the proposed DEM can simulate the relationship debris flow load and time and productivity of the debris flow behavior sufficiently. The maximum debris flow load (45N) by the test and the analysis was larger than the design load (34N).

This method may be applied to estimate the debris flow load acting on the actual steel open dam in the future.

REFERENCES

Daido, A., Yoshizumi, M., and Nakazima, K. (1994): Impact force of mud-debris flows acting on structure, Journal of

hydraulic engineering, Vol.38, pp.557-562 (in Japanese with English abstract).

Ikeya, H. (1987): Classification of an avalanche of earth and rocks, Journal of Civil Engineers, pp.150-155, (in Japanese with English abstract).

Ishikawa, N., Inoue, R., Beppu, M., Hasegawa, Y. and Mizuyama, T. (2009): Impulsive loading test of debris flow model, Proc. of the 8th International Conference on Shock and Impact Loads on Structures, Adelaide, Australia, pp.53-62.

Katsuki, S., Shibuya, H., Ohsumi, H. and Ishikawa, N. (2012): Trap performance analysis of steel open Sabo dam subjected to woody debris by using 3-D DEM, Journal of Japan Society of Civil Engineers, A2 (Applied Mechanics), Vol.69, pp.16-29, (in Japanese with English abstract).

Kiyomiya, O. (2003): Structure Design Overview, Gihodo Publisher, (in Japanese with English abstract).

Miyoshi, I. and Suzuki, M. (1990), Experimental study on impact load on a dam due to debris flow, Journal of the Japan Society of Erosion Control Engineering, Vol.43, No.2(169), pp.11-19, (in Japanese with English abstract).

Mizuyama, T. (1979): Estimation of debris flow impact load against check dam and Its problems, Journal of the Japan Society of Erosion Control Engineering, Vol.32, No.1, pp.40-43, (in Japanese).

Osanai, N., Mizuno, H. and Mizuyama, T. (2010): Design Standard of Control Structures Against Debris Flow in Japan, Journal of Disaster Research, Vol.5, No.3, pp.307-314.

Sabo & Landslide Technical Center (2016): Actual conditions of a landslide disaster in 2016, pp.1-42, (in Japanese).

Shibuya, H., Katsuki, S., Kokuryo, H., Ohsumi, H. and Ishikawa, N. (2012): Experimental study of load for steel open Sabo dam caused by debris flow with woody debris, Journal of the Japan Society of Erosion Control Engineering, Vol.65, No.1, pp.54-61, (in Japanese with English abstract).

Yamamoto, A., Yamamoto, S., Torihira, M. and HIRAMA, K. (1998): Impact load on Sabo dam due to debris flow, Journal of the Japan Society of Erosion Control Engineering, Vol.51, No.2, pp.22-30, (in Japanese with English abstract).